Astronomy & Astrophysics

NGTS-30 b/TOI-4862 b: An ∼1 Gyr old 98-day transiting warm Jupiter[⋆,⋆⋆]

M. P. Battley[1], K. A. Collins[2], S. Ulmer-Moll[1,3], S. N. Quinn[2], M. Lendl[1], S. Gill[4,5], R. Brahm[6,7,8],
M. J. Hobson[1], H. P. Osborn[3], A. Deline[1], J. P. Faria[1], A. B. Claringbold[3,4], H. Chakraborty[1], K. G. Stassun[9],
C. Hellier[10], D. R. Alves[11], C. Ziegler[12], D. R. Anderson[13], I. Apergis[4,5], D. J. Armstrong[4,5],
D. Bayliss[4,5], Y. Beletsky[14], A. Bieryla[2], F. Bouchy[1], M. R. Burleigh[15], R. P. Butler[16], S. L. Casewell[15],
J. L. Christiansen[17], J. D. Crane[18], P. A. Dalba[19], T. Daylan[20], P. Figueira[1], E. Gillen[21], M. R. Goad[15],
M. N. Günther[22], B. A. Henderson[15], T. Henning[23], J. S. Jenkins[24,25], A. Jordán[6,7,8], S. Kanodia[16], A. Kendall[15],
M. Kunimoto[26,⋆⋆⋆], D. W. Latham[2], A. M. Levine[26], J. McCormac[4,5], M. Moyano[13], A. Osborn[4,5], D. Osip[14],
T. A. Pritchard[27], A. Psaridi[1], M. Rice[28], J. E. Rodriguez[29], S. Saha[24,25], S. Seager[26,30,31], S. A. Shectman[18],
A. M. S. Smith[32], J. K. Teske[33], E. B. Ting[34], S. Udry[1], J. I. Vines[13], C. A. Watson[35], R. G. West[4,5],
P. J. Wheatley[4,5], J. N. Winn[36], S. W. Yee[36], and Y. Zhao[1]

(Affiliations can be found after the references)

ABSTRACT

Context. Long-period transiting exoplanets bridge the gap between the bulk of transit- and Doppler-based exoplanet discoveries, providing key insights into the formation and evolution of planetary systems. The wider separation between these planets and their host stars results in the exoplanets typically experiencing less radiation from their host stars; hence, they should maintain more of their original atmospheres, which can be probed during transit via transmission spectroscopy. Although the known population of long-period transiting exoplanets is relatively sparse, surveys performed by the Transiting Exoplanet Survey Satellite (TESS) and the Next Generation Transit Survey (NGTS) are now discovering new exoplanets to fill in this crucial region of the exoplanetary parameter space.

Aims. This study aims to characterise a new long-period transiting exoplanet by following up on a single-transit candidate found in the TESS mission.

Methods. The TOI-4862 system was monitored using a combination of photometric instruments (TESS, NGTS, and EulerCam) and spectroscopic instruments (CORALIE, FEROS, HARPS, and PFS) in order to determine the period, radius, and mass of the long-period transiting exoplanet NGTS-30 b/TOI-4862 b. These observations were then fitted simultaneously to determine precise values for the properties and orbital parameters of the exoplanet, as well as the refined stellar parameters of the host star.

Results. We present the discovery of a long-period ($P = 98.29838 \pm 0.00010$ day) Jupiter-sized ($0.928 \pm 0.032\ R_J$; $0.960 \pm 0.056\ M_J$) planet transiting a 1.1 Gyr old G-type star, one of the youngest warm Jupiters discovered to date. NGTS-30 b/TOI-4862 b has a moderate eccentricity ($0.294^{+0.014}_{-0.010}$), meaning that its equilibrium temperature can be expected to vary from 274^{+30}_{-46} K to 500^{+55}_{-84} K over the course of its orbit. Through interior modelling, NGTS-30 b/TOI-4862 b was found to have a heavy element mass fraction of $0.23^{+0.05}_{-0.06}$ and a heavy element enrichment ($Z_p/Z_\star$) of 20^{+5}_{-6}, making it metal-enriched compared to its host star.

Conclusions. NGTS-30 b/TOI-4862 b is one of the youngest well-characterised long-period exoplanets found to date and will therefore be important in the quest to understanding the formation and evolution of exoplanets across the full range of orbital separations and ages.

Key words. methods: data analysis – planets and satellites: detection – planets and satellites: gaseous planets – planets and satellites: general – planets and satellites: individual: NGTS-30 b – planets and satellites: individual: TOI-4862 b

1. Introduction

Three decades of exoplanet discovery have revealed a population of exoplanets far more diverse than originally anticipated. This diversity is shaped by a combination of formation processes (e.g. Boss 1997; Safronov 1972; Lissauer 1993), planetary migration (e.g. Ward 1986; Lin & Papaloizou 1986; Kozai 1962; Lidov 1962), atmospheric evolution (e.g. Owen 2019), and dynamical interactions (e.g. Ida & Lin 2010), which leave distinct imprints on the overall distribution of exoplanets. One particularly interesting type of exoplanet is 'warm Jupiters', planets with masses and radii approximately that of Jupiter and periods of 10–200 days, which bridge the gap between the short-period 'hot Jupiters' ($P < 10$ days) commonly found in transit surveys and the gas giants in the Solar System. These exoplanets are particularly interesting for studying the evolution and atmospheres of giant planets, as, like the giants in the Solar System, they are found much farther from their host stars and hence are not subject to the intense radiation environments of hot Jupiters

---

(Showman et al. 2020). Likewise, this increased distance means that they are tidally detached from their host stars, so they can offer more clues about their formation environments (Rice et al. 2022). This aspect is especially important to explore as there is some evidence that they may have undergone less migration than close-in exoplanets (Boley et al. 2016; Wu & Lithwick 2011; Bitsch et al. 2019).

The dominant drivers behind the formation and evolution of warm Jupiters are still not well understood (e.g. Müller & Helled 2023). Three particularly important parameters that can be used to constrain these processes are the density, eccentricity, and age of warm Jupiters, which directly probe both the current state, ongoing mechanisms, and timescale of this evolution. The precise density retrieved from measurements of the mass and radius of an exoplanet allows the bulk metallicity of these planets to be estimated and, through comparison to synthetic models, allows a first look at the current internal structure of the exoplanet (e.g. Mordasini et al. 2012, 2015). Meanwhile, eccentricity measurements give insight into how warm Jupiters reached their current orbital position, with low-eccentricity exoplanets best explained by in situ formation or disk migration (e.g. Safronov 1972; Lissauer 1993; Ward 1986) and high-eccentricity exoplanets suggestive of high-eccentricity evolution mechanisms (e.g. Kozai 1962; Lidov 1962). Finally, measurements of the ages of such exoplanets allow them to be placed more effectively on their evolution tracks; this helps us understand whether the observed systems probe the final states of such planets or one that is still actively evolving. This is particularly crucial for high-eccentricity warm Jupiters, which may be in an intermediary evolution state on the way to hot Jupiter formation (Fabrycky & Tremaine 2007). To date, ages have been determined with precision better than 50% for 24 well-constrained warm Jupiters. However, the majority of these are older (>5Gyr) and have periods of <60 days. To determine the dominant drivers shaping warm Jupiters, it is vital that a well-characterised sample of such exoplanets across their full evolutionary history be assembled.

Due to the geometric probability of a transit being inversely proportional to the orbital distance, the largest number of longer-period exoplanets have been found via the radial velocity (RV) method (e.g. Udry et al. 2003; Marmier et al. 2013; Borgniet et al. 2019). However, as different discovery methods allow for the determination of different planetary parameters, in-depth characterisation of exoplanets relies on combining different discovery methods. Crucially, the RV method alone cannot give the radius of an observed exoplanet and can only give the minimum mass of an exoplanet ($M_P \sin i$). The optimal way to solve this problem is to observe the transit of such a planet around its host star and determine the radius of the planet from the depth of the transit (Borucki & Summers 1984). Combining these methods provides us with precise constraints on the density and composition of such planets. However, with fewer than 50 well-constrained warm Jupiters with precise masses and radii ($\sigma_{M_P}/M_P \leq 25\%$; $\sigma_{R_P}/R_P \leq 8\%$) currently known[1], a larger sample of such planets is needed.

Long-period transiting exoplanets are particularly valuable because their atmospheres can be studied through transmission spectroscopy (Seager & Sasselov 2000), which directly probes their chemical composition. The moderate-temperature atmospheres of long-period planets (between well-studied hot Jupiters and Solar System gas giants) are predicted to host a range of observationally unconstrained atmospheric processes. Transmission spectroscopy of temperate gas giants can probe transitions in nitrogen chemistry (e.g. Fortney et al. 2020; Hu 2021; Ohno & Fortney 2023) and aerosol properties (e.g. Pont et al. 2008; Gao et al. 2017; Brande et al. 2024), which are essential for understanding the entirety of the gas giant parameter space. By measuring the atmospheric composition of gas giants with different orbital architectures, we can hope to understand the formation and migration history of giant planets (e.g. Mordasini et al. 2012; Ohno & Fortney 2023).

Unfortunately, directly looking for transits of known long-period planets discovered from RV measurements is difficult due to the decreased transit probability at these wider separations. A more efficient method is to look for long-period transiting exoplanet candidates with ongoing all-sky transit surveys such as the Transiting Exoplanet Survey Satellite (TESS; Ricker et al. 2014) and measure their masses via RV follow-up. As TESS typically observes each region of the sky for only a month at a time, any long-period exoplanets are usually found as single-transit candidates – or 'mono-transits' – requiring additional follow-up to determine their periods. Cooke et al. (2018) and Villanueva et al. (2019) using similar techniques as Osborn et al. (2016) each demonstrated that hundreds of such long-period planets should be detectable as single transits in the TESS Primary mission alone.

These predictions have led to several mono-transit-specific searches in TESS data (e.g. Gill et al. 2020; Montalto et al. 2020) as well as those highlighted as TESS objects of interest (TOIs; Guerrero et al. 2021) in the main search completed by the TESS mission (Ricker et al. 2014; Jenkins et al. 2016). In order to confirm a long-period exoplanet from a mono-transit, one must first determine the orbital period. This can be achieved through additional photometric monitoring, spectroscopic follow-up over a complete period, or some combination of the two (e.g. Lendl et al. 2020). If a second transit is observed some time later around the star with the same depth and shape (but with a time gap), then it becomes a 'duo-transit', and the true period is restricted to a set of period aliases that can be efficiently checked through follow-up photometry (e.g. Osborn et al. 2022). These duo-transits became increasingly common after the completion of the TESS primary mission in July 2020, as the TESS mission was extended to approximately switch between the northern and southern hemispheres year by year[2]. However, because typically only one month of data are collected for each region of the sky by TESS every two years, this still misses the majority of long-period transiting exoplanets. Confirming these systems in a more efficient manner necessitates more targeted follow-up with both photometry and spectroscopy (Cooke et al. 2020).

The first transiting planet to be discovered from a mono-transit in TESS data was NGTS-11 b (TOI-1847 b), a warm Saturn in a 35.46-day orbit around a K-type star (Gill et al. 2020). The first sign of this planet was a single transit in TESS data; a second transit was found from 79 nights of monitoring observations with the Next Generation Transit Survey (NGTS; Wheatley et al. 2018), which ruled out all but 13 remaining possible periods and allowed the final period to be determined through joint fits to the transit and collected RV data. Since this first discovery, long-period exoplanet discoveries based on single transits in TESS data have multiplied, with over a dozen discovered in the last two years alone (Dalba et al. 2020; Ulmer-Moll et al. 2022, 2023; Grieves et al. 2022;

---

[1] https://exoplanetarchive.ipac.caltech.edu/

[2] See https://tess.mit.edu/observations/ for full details of the pointing by sector.

Gupta et al. 2023; Brahm et al. 2023; Mireles et al. 2023; Mann et al. 2023; Osborn et al. 2023).

This paper describes the discovery and characterisation of a new ~1Gyr old transiting warm Jupiter detected from only one full and a two partial transits, supported by high-precision mass measurements made using CORALIE, the Fiber-fed Extended Range Optical Spectrograph (FEROS), the High Accuracy Radial velocity Planet Searcher (HARPS), and the Carnegie Planet Finder Spectrograph (PFS). The observations of this target and its host star are summarised in Sect. 2, followed by a description of the derivation of stellar parameters, initial photometric and spectroscopic analyses, and the joint modelling in Sect. 3. The final results are presented and discussed in Sect. 4, before the paper concludes in Sect. 5.

2. Observations

NGTS-30 b/TOI-4862 b was first discovered via a single transit in TESS photometry (Sect. 2.1), before archival photometry from NGTS (see Sect. 2.2) and EulerCam (Sect. 2.3) were used to refine the planetary period. Ground-based spectroscopic observations were obtained using the high resolution spectrographs CORALIE (Sect. 2.5), FEROS (Sect. 2.6), HARPS (Sect. 2.7), and PFS (Sect. 2.8). Speckle imaging observations to check for other nearby sources were taken using the Southern Astrophysical Research (SOAR) telescope (Sect. 2.9).

2.1. TESS photometry

TESS observed TOI-4862 (TIC 322807371) during three different sectors in Years 1, 3, and 5 of its observations: Sector 9 (28 February 2019 to 26 March 2019), Sector 36 (7 March 2021 to 2 April 2021) and Sector 63 (10 March 2023 to 6 April 2023). In Sector 9, it was observed in 30-minute cadence in the TESS Full Frame Images (FFIs), but increased to 10-minute cadence in Sector 36 and 200-second cadence in Sector 63. Because of the long period of this exoplanetary system, only a single transit of TOI-4862 b was seen in the TESS photometry, occurring at barycentric dynamical time (BJD) 2459287.6 in the Sector 36 observations (n.b. all times are in the barycentric dynamical time frame). This single transit was originally found as part of the Quick-Look Pipeline (QLP) faint star search (Kunimoto et al. 2023) resulting in a TOI alert on 21 December 2021. This transit event is shown in Fig. 1.

To rule out possible false positive scenarios for this single transit such as asteroids or background effects, the TESS calibrated Full-Frame-Images were carefully inspected, confirming that the signal came from the star TOI-4862. Furthermore, *Gaia* DR3 results from the surrounding region were reviewed to ensure that the signal could not come from nearby blended stars, planets or eclipsing binaries. No other stars brighter than *Gaia* mag 16.5 were found within the aperture used for TESS photometry. Before being elevated to a TOI by the TESS team, the candidate signal was carefully vetted to rule out clear systematic effects, binaries, astrophysical variability, non-transit shaped signals or signals with clear differences between even and odd transits, as outlined by Guerrero et al. (2021). Following elevation, the candidate signal was given the name TOI-4862.01.

TESS light curves of TOI-4862 were obtained from the *Mikulski* Archive for Space Telescopes[3], accessing the light curves analysed by the TESS Science Processing Operations

Centre (SPOC; Jenkins et al. 2016, located at NASA Ames Research Center). The TESS-SPOC high level science product FFI light curves were used (Caldwell et al. 2020). The Presearch Data Conditioning Simple Aperture Photometry (PDC_SAP) fluxes and errors were used for this analysis (Stumpe et al. 2012, 2014; Smith et al. 2012). PDC_SAP light curves are extracted via aperture photometry from calibrated target pixel files and correct for dilution and systematic trends. The SPOC conducted a transit search in the TESS-SPOC light curve for Sector 36 with a noise-compensating matched filter (Jenkins 2002; Jenkins et al. 2020), which yielded the detection of the single transit of TOI-4862. A limb-darkened model was fitted to the light curve (Li et al. 2019) and a suite of diagnostic tests were conducted to make or break confidence in the transiting planet hypothesis (Twicken et al. 2018), including the difference image centroiding test, which located the host star within 0.9 ± 2.5 arcsec of the transit source location. We note, however, that only data from Sector 36 data were used in the joint fit as it was the only sector containing a transit. No significant periodic stellar activity was evident in the TESS photometry for this target.

2.2. NGTS photometry

Following the detection of the single transit of TOI-4862 b by TESS, archival data from the NGTS (Wheatley et al. 2018) was searched, in case additional transits of this long-period planet had been independently observed. This process revealed that NGTS had 135 nights of existing archival photometry for TOI-4862 b (see Fig. 2), including an ingress of the same depth and shape as the single transit in TESS from 2016 (BJD 2457419.9, see Fig. 1). NGTS comprises 12 automated 20 cm telescopes located at the Paranal site of the European Southern Observatory (ESO). Data are typically taken with one telescope at a time in blind-survey mode, but this can be increased to several telescopes for important transits (e.g. see Bryant et al. 2020; Smith et al. 2020). Specially designed to search for transiting exoplanetary signals from the ground, NGTS is capable of high-precision photometry that matches TESS (in regard to precision) for $T_{mag} > 12$ for a single telescope and $T_{mag} > 9$ for multiple telescopes observing concurrently (Bryant et al. 2020). All NGTS data are acquired with exposure times of 10 s and a cadence of 13 s. Magnitude data were extracted from the telescope using the standard NGTS aperture photometry extraction pipeline and systematics removal detailed in Wheatley et al. (2018). Following extraction of the light curves, transits were searched for using the template-matching technique described in Gill et al. (2020).

As the archival NGTS data included only a single ingress for this target, additional observations were performed between February 2022 and July 2023 in order to search for additional transits and constrain the period further. This resulted in another 125 nights of data, for a total of 260 nights of data between November 2015 and July 2023 for TOI-4862. Although no additional transits were found in this search, the resulting extensive dataset allowed the majority of the possible period aliases for the planet candidate to be ruled out, as discussed in Sect. 3.2. All NGTS monitoring data are plotted in Fig. 2, excluding those nights that were hampered by poor observing conditions and a further four nights that were taken on different NGTS telescopes.

2.3. EulerCam photometry

In the final stages of preparing this paper, the opportunity arose to observe an additional transit of TOI-4862 b with EulerCam on the night of 27 February 2024, aligning with the most likely
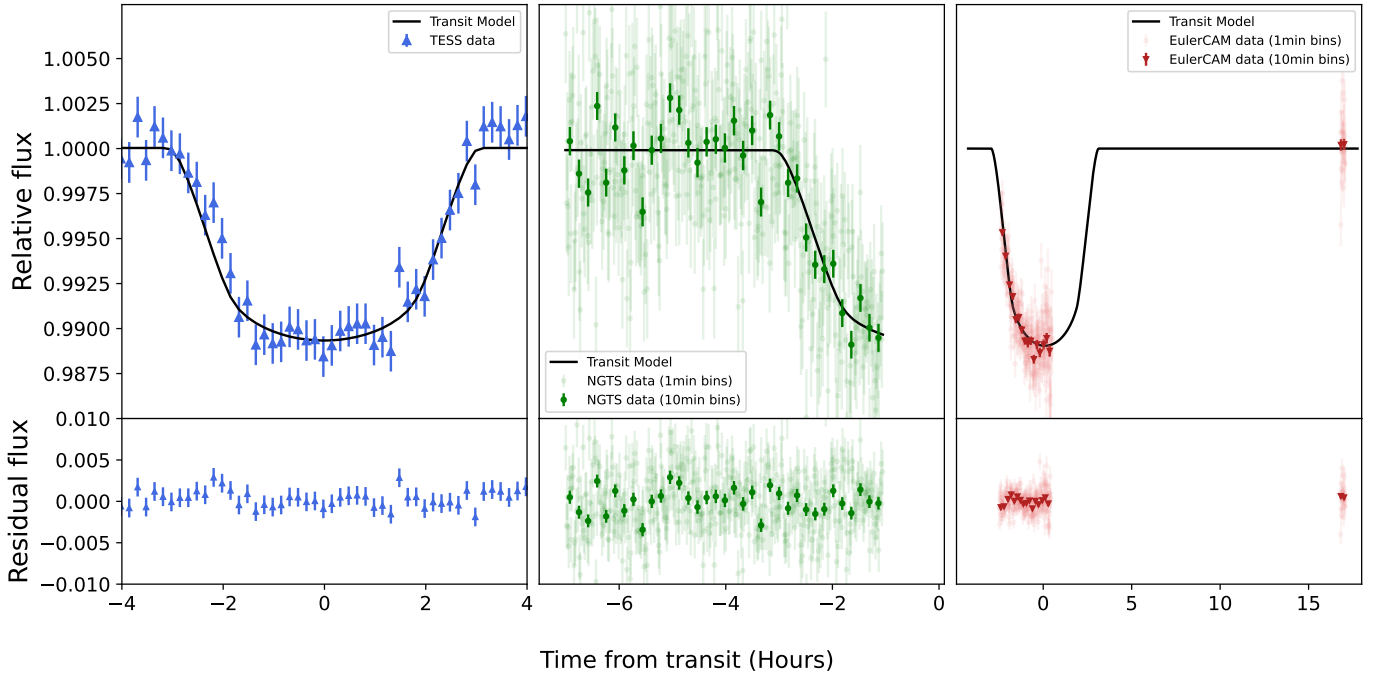
---

[3] https://mast.stsci.edu/portal/Mashup/Clients/Mast/Portal.html

Fig. 1. Fitted transits from TESS (left), NGTS (middle), and EulerCam (right) along with their residuals after removing the transit model (lower panels). Because of the high-cadence of the NGTS and EulerCam data, data are shown binned to 1 minute (in lighter colours) and 10 minute bins (darker colours) to align with the TESS data. The joint transit model is over-plotted in black.
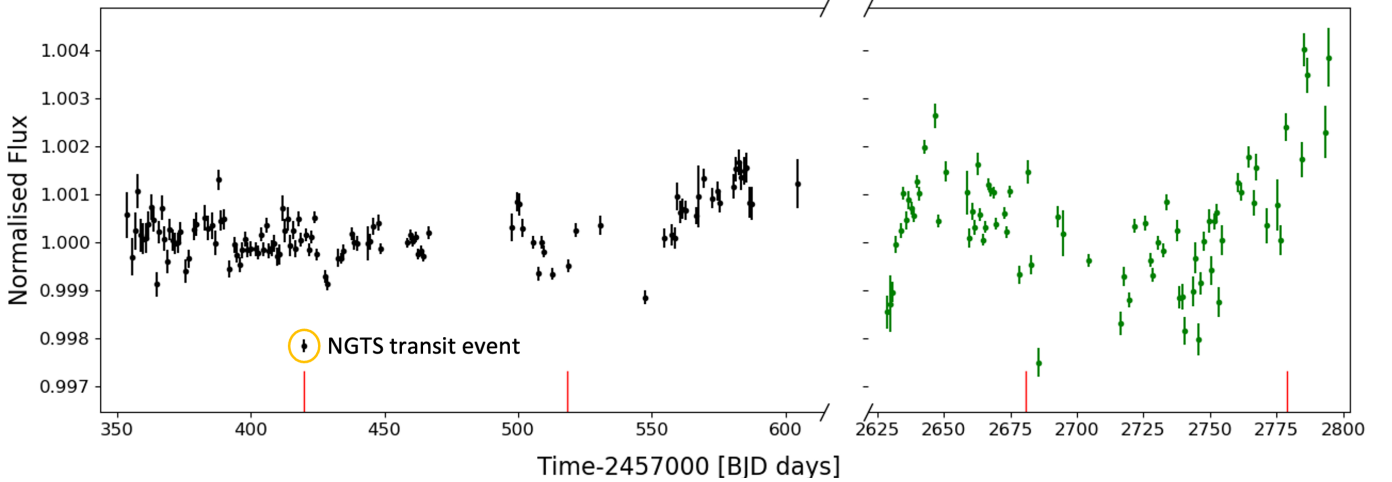

Fig. 2. NGTS monitoring plot showing average nightly fluxes for TOI-4862. Archival NGTS data (from before the TESS transit) are plotted in black, and follow-up monitoring is plotted in green with 1-σ flux errors. Measurements obtained on nights overly affected by noise or weather as well as four monitoring points from different NGTS telescopes with different offsets are not shown. Red lines denote the expected times of transit for NGTS-30 b/TOI-4862-b, with the first one aligning with the captured NGTS transit (circled). Nightly errors are generally higher in the newer datasets because the typical observation lengths were shorter in this monitoring stage.

period alias of 98.3 days. As all points from this observation where during the transit, an additional follow-up observation was also carried out the following night (28 February 2024) to confirm the out of transit flux baseline.

EulerCam is a 4k × 4k CCD detector installed in the 1.2 m *Leonhard Euler* Telescope at ESO's La Silla Observatory (Lendl et al. 2012). The observations were acquired in the NGTS filter with an exposure time of 30 s and 0.1 mm de-focus. The raw full-frame images are corrected for bias, over-scan and flat field using the standard EulerCam reduction pipeline. The aperture photometry is performed by placing circular apertures of varying radii on the target and a few reference stars. The exact placement of these apertures is performed using the astrometric solution of

stars in the field-of-view (Lang et al. 2010). The optimal aperture size and reference stars are selected by minimising the root mean square scatter of the light curve, which in this case was 40 pixels.

This new observation showed a partial transit with the same depth and shape as the TESS and NGTS transits (as shown in Fig. 1), confirming that the 98.3 day period alias was the true period.

2.4. TRES reconnaissance spectroscopy

Two reconnaissance spectra were obtained with the Tillinghast Reflector Echelle Spectrograph (TRES; Furész 2008) located at the *Fred Lawrence Whipple* Observatory (FLWO) on

16 February 2022 and 15 March 2022. TRES is a fibre-fed echelle spectrograph operating in the 3900–9100 Å wavelength range with a spectral resolution of $R = 44\,000$. The spectra were extracted and reduced following procedures outlined in Buchhave et al. (2010) and used to derive stellar parameters using the Stellar Parameter Classification (SPC) tool (Buchhave et al. 2014). SPC derives an effective temperature, surface gravity, metallicity, and rotational velocity by cross-correlating the observed spectra against Kurucz atmospheric models (Kurucz 1992). The derived stellar parameters were: $T_{\rm eff} = 5479 \pm 50$ K, $\log g = 4.60 \pm 0.10$, $[{\rm m/H}] = 0.03 \pm 0.08$, $v \sin i = 3.3 \pm 0.5$ km s^{-1} and a signal to noise per resolution element of SNRe = 28.1. We note, however, that because only two spectra were obtained by TRES, these data are not included in the full RV analysis.

2.5. CORALIE spectroscopy

TOI-4862 was added to an existing programme on the CORALIE spectrograph (Queloz et al. 2000) to follow up on long-period transiting exoplanet candidates from TESS. CORALIE is a fibre-fed echelle spectrograph installed at the Swiss 1.2 m *Leonhard Euler* Telescope at the La Silla site of the ESO in Chile. The CORALIE spectrograph uses two fibres for fibre injection: the first is dedicated to observing the target, and the second can focus on either light from a Fabry-Pérot etalon to perform simultaneous drift calibration or the sky to allow for background subtraction. In this case, the Fabry-Pérot etalon was used. Spectra were extracted from the detector using the standard CORALIE calibration reduction pipeline, before RV measurements were determined through cross-correlation with a binary G2 mask (Pepe et al. 2002). In total 20 CORALIE spectra of TOI-4862 were taken between 19 January 2022 and 28 June 2023, with exposure times of 30–45 min depending on observing conditions. The extracted RV measurements had an overall dispersion of <70 ms^{-1}, providing good evidence that the observed transit signal came from a planetary-mass object. All CORALIE RV measurements are plotted in Fig. 3 and can be found in Table 1.

2.6. FEROS spectroscopy

Following the beginning of the CORALIE observations, nine additional spectra were obtained using the FEROS spectrograph. FEROS is a high resolution spectrograph installed on the 2.2 m telescope at the La Silla site of the ESO (Kaufer et al. 1999). FEROS has a spectral resolution of 48 000, corresponding to 2.2 pixels of 15 μm, and covers the wavelength range of 3600–9200 Å. The eight FEROS spectra were collected between 10 March 2022 and 5 July 2022 as part of the ongoing programme to follow up long-period planets (PI: Hobson; ESO Program ID 0108.A-9003(A) and 0109.A-9003(A)). All data were taken using an exposure time of 1500 s. Radial velocity measurements were then extracted from each spectrum using the cross-correlation technique, according to the CERES pipeline outlined in Brahm et al. (2017). These RV measurements are summarised in Table 1 and plotted in Fig. 3.

2.7. HARPS spectroscopy

In order to more precisely constrain the mass of NGTS-30 b/TOI-4862 b, 19 spectra were obtained for TOI-4862 on the HARPS spectrograph (Pepe et al. 2002). HARPS is a fibre-fed spectrograph installed on the 3.6 m telescope at La Silla. It has
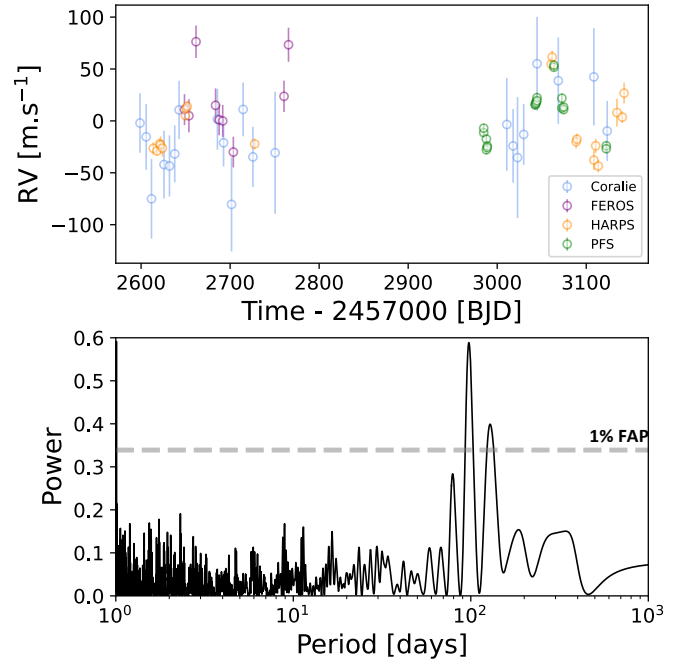

Fig. 3. Overview of collected RV data Top: all collected RV observations for TOI-4862. CORALIE points are shown in blue, FEROS in purple, HARPS in orange, and PFS in green. All points are shown as empty circles, with their 1σ errors shown as straight lines. Inter-instrument offsets have been removed. Bottom: Lomb-Scargle periodogram for the collected RV observations. The 1% false alarm probability (FAP) is shown by the dotted grey line. The highest peak corresponds to a period of about 97.4 days.

Table 1. RV data for TOI-4862.

Time BJD	RV (m s^{-1})	RV error (m s^{-1})	Instrument –
2459598.79120	−3.66	28.607552	CORALIE
2459605.74120	−16.97	31.680687	CORALIE
2459611.69435	−76.67	38.410280	CORALIE
...	...	...	...
2460074.59522	13.6	8.0	PFS
2460122.49911	−23.68	2.05	PFS
2460122.51344	−26.59	2.08	PFS

Notes. The full table of RV data is available at the CDS.

a spectral resolution of ~115 000 and covers the wavelengths of 3800–6900 Å. The observations of TOI-4862 were taken as part of ongoing long-period transiting giants programmes (108.22L8, 109.23J8 & 111.250B, PI: Ulmer-Moll). TOI-4862 was observed in the high-accuracy mode between 3 February 2022 and 17 July 2023, with exposure times of 1800 s. All HARPS data were reduced using version 3.0 of the standard HARPS reduction pipeline (Lovis & Pepe 2007). Radial velocities were then extracted from these spectra through cross-correlation with a G2 mask. These RV measurements are summarised in Table 1 and plotted in Fig. 3.

2.8. PFS spectroscopy

Twenty additional RV measurements of TOI-4862 were taken concurrently by the Carnegie PFS (Crane et al. 2006, 2008,
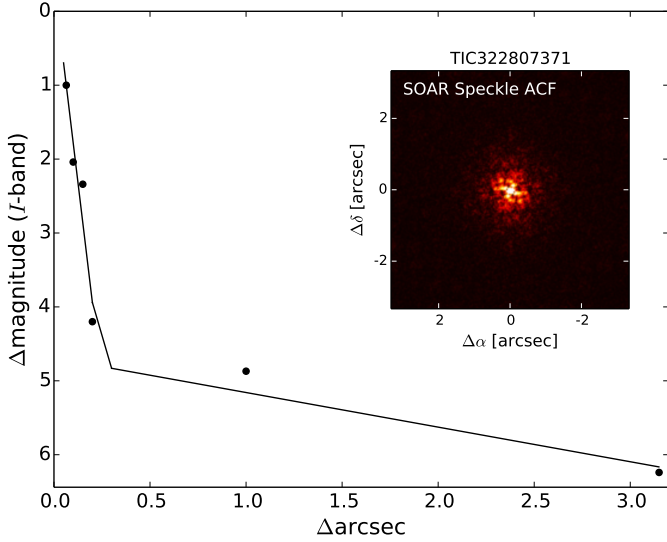
Fig. 4. SOAR speckle-imaging observations of TOI-4862. No additional sources were observed within 3″ of the target.

2010). PFS is a high-precision echelle spectrograph attached to the 6.5 m *Magellan Clay* telescope at Las Campanas Observatory in Chile. It has a spectral resolution of ∼130 000 and covers the 3900–7340 Å spectral window. Wavelength calibration is carried out using an iodine absorption cell, which also allows for the characterisation of the instrumental profile. Spectra were reduced using the standard PFS reduction pipeline (Butler et al. 1996; Crane et al. 2006) and RV measurements were extracted using a custom IDL pipeline. TOI-4862 was observed by PFS between 9 February 2023 and 27 June 2023, for a total of 20 individual measurements. All PFS RV measurements are summarised in Table 1 and plotted in Fig. 3.

2.9. SOAR speckle imaging

High-angular resolution imaging is needed to search for nearby sources that can contaminate the TESS photometry (resulting in an underestimated planetary radius) or be the source of astrophysical false positives such as background eclipsing binaries. A search for stellar companions to TOI-4862 was done with speckle imaging on the 4.1 m SOAR telescope (Tokovinin 2018) on 20 March 2022 UT in the Cousins *I*-band, a band-pass similar to that of a TESS camera. This observation was sensitive to a 5.0-magnitude fainter star at an angular distance of 1 arcsec from the target, but no nearby stars were detected within 3″ of TOI-4862. More details of the observations within the SOAR TESS survey are available in Ziegler et al. (2019). The 5σ detection sensitivity and speckle auto-correlation functions from the observations are shown in Fig. 4.

3. Data analysis

3.1. Stellar parameter determination

The collected HARPS spectra were used to determine the properties of the host star TOI-4862, co-adding the 15 spectra by correcting them to a common wavelength scale and combining them to a single spectrum with signal-to-noise of ∼90. Following Gill et al. (2020), the ISPEC (Blanco-Cuaresma et al. 2014) and SPECTRUM (Gray 1999) codes were used to model a grid of synthetic spectra based on MARCS model atmospheres (Gustafsson et al. 2008), version 5 of the *Gaia*-ESO Survey
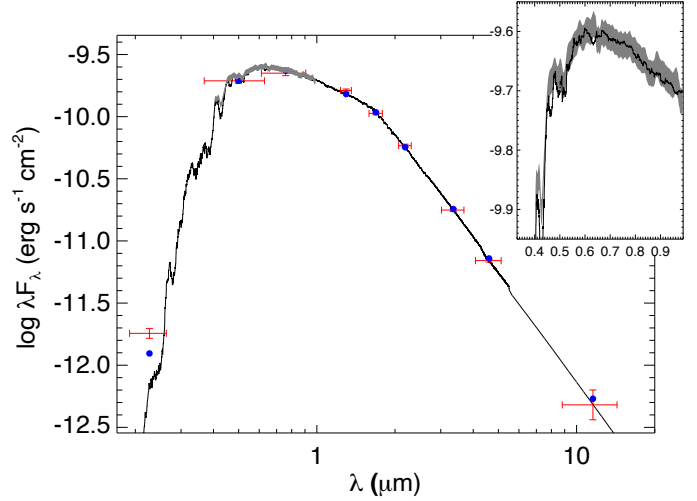
Fig. 5. Spectral energy distribution of TOI-4862. Red symbols represent the observed photometric measurements, and the horizontal bars represent the effective width of the passband. Blue symbols are the model fluxes from the best-fit PHOENIX atmosphere model (black). The absolute flux-calibrated *Gaia* spectrum is shown as a grey swathe in the inset figure. We note that the discrepancy between the blue points and PHOENIX atmosphere model at the shortest wavelengths is due to the SED being so steep in the UV that the nominal band-pass effective wavelength ends up being different from the flux-weighted effective wavelength.

atomic line lists and solar abundances from Asplund et al. (2009). Based on these models, the stellar effective temperature, $T_{\rm eff}$, and stellar surface gravity, log g, were calculated from the Hα, NaI D, and MgI b lines, while the metallicity, Fe/H, and rotational broadening, $v \sin i$, were determined from the individual FeI and FeII lines.

An analysis of the broadband spectral energy distribution (SED) of the star was performed together with the *Gaia* DR3 parallax, in order to determine an empirical measurement of the stellar radius (Stassun & Torres 2016; Stassun et al. 2017, 2018). The JHK_S magnitudes were sourced from 2MASS, the $W1$–$W3$ magnitudes from WISE, the $G_{\rm BP}$ and $G_{\rm RP}$ magnitudes from *Gaia*, and the near-UV magnitude from GALEX. The absolute flux-calibrated *Gaia* spectrum was also utilised. Together, the available photometry spans the full stellar SED over the wavelength range 0.2–10 μm (see Fig. 5).

A fit using PHOENIX stellar atmosphere models (Husser et al. 2013) was performed, adopting from the spectroscopic analysis the effective temperature ($T_{\rm eff}$), metallicity ([Fe/H]), and surface gravity (log g). The extinction A_V was fitted for, limited to the maximum line-of-sight value from the Galactic dust maps of Schlegel et al. (1998). The resulting fit (Fig. 5) has $A_V = 0.11 \pm 0.06$. Integrating the (un-reddened) model SED gives the bolometric flux at Earth, $F_{\rm bol} = 3.628 \pm 0.085 \times 10^{-10}$ erg s^{-1} cm^{-2}. Taking the $F_{\rm bol}$ together with the *Gaia* parallax directly gives the bolometric luminosity, $L_{\rm bol} = 0.663 \pm 0.016$ $L_\odot$. The Stefan-Boltzmann relation then gives the stellar radius, $R_\star = 0.913 \pm 0.029$ $R_\odot$. In addition, the stellar mass was estimated using the empirical relations of Torres et al. (2010), giving $M_\star = 0.94 \pm 0.06$ $M_\odot$.

Finally, the projected stellar rotation period, $P_{\rm rot}/\sin i$, was estimated from the spectroscopic $v \sin i$ together with $R_\star$, giving 13.2 ± 3.0 days. From the empirical gyrochronology relations of Mamajek & Hillenbrand (2008), the system age can then be estimated to be 1.1 ± 0.4 Gyr. Curiously, although no reliable
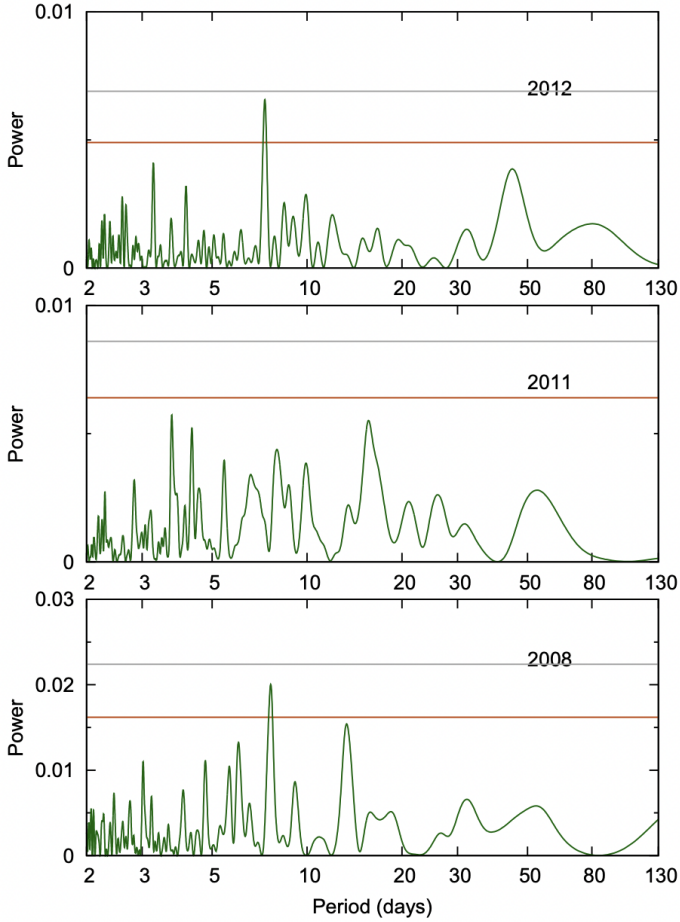
Fig. 6. WASP rotation analysis: Lomb-Scargle periodograms were run for three separate years of WASP photometry, in 2012, 2011, and 2008 (from top to bottom). 1% and 10% false alarm probability levels (estimated with methods from Maxted et al. 2011) are shown as grey and red lines, respectively. The same ~7.5 days rotation signal is marginally detected in 2012 and 2008, while the highest peak in the 2011 data is at 3.73 days, which could be a harmonic of the 7.5 days signal.

rotation period was retrieved from the NGTS monitoring data (nor in the TESS sectors), archival longer-term photometric monitoring by the Wide Angle Search for Planets (WASP) survey (Pollacco et al. 2006) marginally detected a shorter period of 7.5 ± 0.3 days (see Fig. 6), which matches the value from $v \sin i$ if $i \sim 35°$. This would suggest that the planet's orbit is misaligned with the stellar spin axis, and would also lead to a gyrochronological age even younger than 1.1 Gyr. Given the young age of this target, further observations to more reliably determine the rotation period and (mis)alignment of the star would be highly valuable.

All stellar properties extracted from this analysis can be found in Table 2 and are in good agreement with both those in version 8 of the TESS Input Catalogue (Stassun et al. 2019) and those extracted from the TRES spectra on ExoFOP[4].

3.2. Photometric analysis

As only one transit of NGTS-30 b/TOI-4862 b was found in the TESS data and only an ingress was recovered in the NGTS data,

[4] https://exofop.ipac.caltech.edu/tess/target.php?id=322807371

Table 2. Stellar names, properties, and photometric magnitudes.

Parameter	Value	Source
Names		
TOI	TOI-4862	TESS
TIC ID	322807371	TESS
2MASS ID	J11345152-2436189	2MASS
Gaia DR3 ID	3533836281547278848	*Gaia*
Astrometric properties		
RA	11:34:51.57	*Gaia*
Dec	−24:36:19.75	*Gaia*
pmRA (mas yr^{-1})	23.7449 ± 0.0119	*Gaia*
pmDec (mas yr^{-1})	−49.3001 ± 0.0109	*Gaia*
Parallax (mas)	4.1305 ± 0.0157	*Gaia*
Distance (pc)	233.9 ± 1.2	*Gaia*
Magnitudes		
TESS (mag)	11.6707 ± 0.006	TESS
V (mag)	12.537 ± 0.214	*Tycho*
B (mag)	12.221 ± 0.315	*Tycho*
G (mag)	12.1646 ± 0.0001	*Gaia*
J (mag)	10.943 ± 0.023	2MASS
H (mag)	10.601 ± 0.027	2MASS
Ks (mag)	10.501 ± 0.022	2MASS
WISE1 (mag)	10.475 ± 0.023	WISE
WISE2 (mag)	10.512 ± 0.02	WISE
WISE3 (mag)	10.491 ± 0.085	WISE
WISE4 (mag)	8.297	WISE
Bulk properties		
T_{eff} (K)	5455 ± 80	Sect. 3.1
Fe/H (dex)	−0.03 + 0.08	Sect. 3.1
log g (cm s^{-2})	4.3 ± 0.5	Sect. 3.1
$v \sin i$ (km s^{-1})	3.5 ± 0.8	Sect. 3.1
$M_\star$ ($M_\odot$)	0.94 ± 0.06	Sect. 3.1
$R_\star$ ($R_\odot$)	0.913 ± 0.029	Sect. 3.1
Age (Gyr)	1.1 ± 0.4	Sect. 3.1

References. TESS (Stassun et al. 2019); 2MASS (Skrutskie et al. 2006); *Gaia* DR3 (Gaia Collaboration 2016); *Tycho* (Hog et al. 2000); WISE (Wright et al. 2010).

the true period of the planet was initially unknown. In order to determine the separation of the TESS and NGTS transits, the two transits were fit simultaneously with a basic `batman` transit model (Kreidberg 2015), utilising the transit depth from the TESS transit and wide uniform priors on the period. This resulted in a maximum period of $1867.68^{+0.19}_{-0.16}$ days. However, because only two transits existed for this target, many possible period aliases remained, determined from the equation $P_n = 1867.7/n$, where n is an integer. To test each of these aliases, the archival and new photometric data were folded by each alias down to $n = 52$ ($P = 35.9$ days), and those aliases with clearly flat NGTS data were discarded. Given the length of the transit in the TESS data and extensive monitoring by NGTS, any periods shorter than 36 days were already implausible. As aliases were ruled out, the NGTS follow-up was directed to focus solely on epochs of aliases that remained. Following this photometric follow-up, only 6 aliases remained plausible, excluding the original 1867-day period. The remaining period aliases were analysed
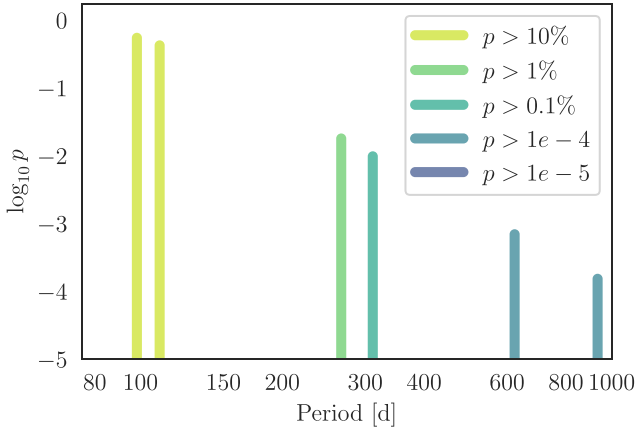
Fig. 7. Most likely period aliases based on the TESS and NGTS photometric fit from the `MonoTools` package ([Osborn et al. 2022](#)). The most favoured remaining period is 98.3 days, aligning with the favoured period from the RV-only period search (Sect. [3.3](#)). The y-axis shows the log likelihood.

using the `MonoTools` package ([Osborn et al. 2022](#)), which performs a Bayesian comparison of the most likely period aliases based on the shape of the transits. This analysis determined that the two shortest remaining periods, 98.3 and 109.9 days, were most favoured as shown in Fig. [7](#). As this manuscript was in the final stages of completion, an additional opportunity arose to observe the most likely alias of 98.3 days with EulerCam on the Swiss 1.2 m *Leonhard Euler* Telescope. This additional observation on 27 February 2024 revealed a transit signal of the same depth as that in TESS and NGTS, confirming that the 98.3 day period was correct through photometric data alone.

3.3. Radial velocity analysis

An independent fit of only the RV data was also completed ahead of the joint analysis, using the `kima` package ([Faria et al. 2018](#)) to search for periodic signals in the combined data from all four spectroscopic instruments. The `kima` package uses Bayesian inference to model a sum of Keplerian signals, and also allows the evidence for different numbers of planets to be easily compared. As an initial test, the number of planets was allowed to vary as a free parameter between zero to two. The `kima` model was run for 100 000 steps with the new level interval set to 3000. This analysis revealed that the one-planet model was the most likely, with the one-planet model ($\ln(Z) = -290.5$, where Z denotes the likelihood) several times more likely than the zero-planet model ($\ln(Z) = -338.6$) and about eight times more likely than the two-planet model ($\ln(Z) = -292.4$). In order to determine the most likely period from the RV data alone, a second `kima` run was completed with a set one-planet model, which suggested that the most likely period was 97 days (as shown in Fig. [8](#)), in good agreement with the most likely period from the photometric-only fit completed in Sect. [3.2](#). Notably, there was no evidence for the second most likely period (109.9 days) from the spectroscopic fit, with the long baseline of the HARPS data effectively ruling out this period alias.

As an independent check, a Lomb-Scargle period search ([Lomb 1976](#); [Scargle 1982](#)) was also carried out, giving a wide peak of maximum likelihood around 97.4 days (see Fig. [3](#)). This gave good confidence that the 98.3 day period was the correct period for NGTS-30 b/TOI-4862 b, allowing this to be used as a prior in the joint fit below. The RV time series for these data
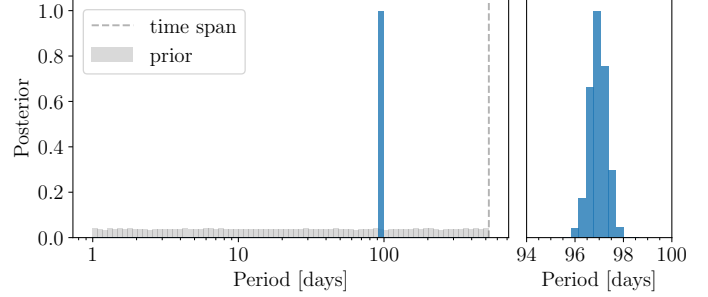
Fig. 8. Posterior distribution (blue) for the orbital period from the `kima` fit of only RV data. The posterior distribution's highest peak corresponds to a period of 97 days. The prior distribution is shown as an extended grey box near the bottom of the plot and is log-uniform from 1 day to the time span of the data at ~500 days, as shown by the dotted grey line.

is shown in Fig. [3](#), alongside the results from the generalised Lomb-Scargle periodogram run on the RV data alone.

3.4. Global modelling

Global modelling for NGTS-30 b/TOI-4862 b was completed using the `juliet` package ([Espinoza et al. 2019](#)). `juliet` combines transit fitting using `batman` ([Kreidberg 2015](#)), RV fitting using `radvel` ([Fulton et al. 2018](#)), Gaussian process modelling with `george` ([Foreman-Mackey et al. 2017](#)) and `celerite` ([Foreman-Mackey et al. 2017](#)), and nested sampling in order to allow it to efficiently and simultaneously fit data from multiple photometric and spectroscopic datasets. Several different nested sampling algorithms are included in the `juliet` package, but in this case `dynesty` ([Speagle 2020](#)) was used to conduct the global modelling. As in the `kima` fit, different RV instruments can be included in the fit by also fitting for the RV offsets between the different datasets.

Alongside the shared parameters such as period, eccentricity, argument of periastron and stellar density, additional terms included in the photometric part of the global model were the impact parameter, radius ratio, mid-transit time (T_0), mean flux offsets and limb-darkening coefficients for each instrument (following the [Kipping 2013](#) parameterisation of q1 and q2), while the spectroscopic part of the model included extra parameters for the RV semi-amplitude and individual spectrograph offsets. Parameters with prior values calculated from the photometric, spectroscopic and/or stellar parameter analysis such as the orbital period, T_0, stellar density, and the mean flux values, were fit with normal distributions around the calculated mean and inflated standard deviations (roughly five times the calculated standard deviation), while unknown parameters were typically allowed to vary across wide but realistic parameter spaces in uniform or log-uniform distributions. A reasonably narrow normal distribution ($\sigma = 1.5$ days) was used as a prior for the 98.3 day period to avoid the other aliased periods ruled out by photometric monitoring but was kept wide enough to account for the slight difference between this photometrically determined period and those from RV measurements alone (~97 days). Meanwhile because neither the NGTS nor EulerCam data contained a full transit, T_0 was taken to be the centre of the TESS single transit. Fitting the stellar density was chosen instead of the scaled semi-major axis (a/R_*). The stellar mass and radius were based directly on the conducted stellar analysis in Sect. [3.1](#), allowing a precise prior to be placed on this parameter. Because the TESS PDCSAP light
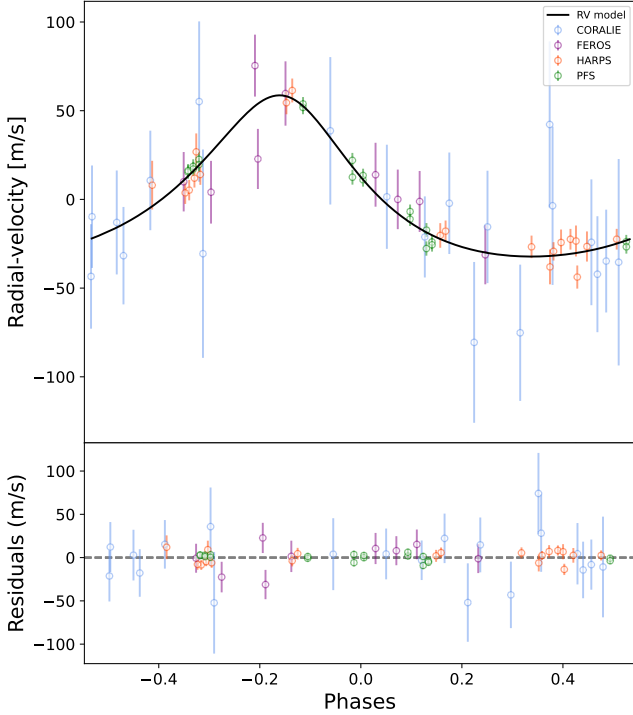
Fig. 9. Phase-folded RV data for the NGTS-30/TOI-4862 system. Top: collected RV data with the joint planet model over-plotted in black. Bottom: RV residuals after subtracting the RV model. For clarity, a dashed grey line is plotted at zero on the residuals plot. The eccentricity of NGTS-30 b/TOI-4862 b's orbit is clearly shown by the asymmetry of the RV model.

curves automatically correct for dilution as part of the extraction pipeline, the dilution factor for TESS was not included in the fit. Likewise, because of the much smaller pixel sizes of the NGTS and EulerCam detectors, these light curves were not found to be affected by dilution either, so the dilution term was also fixed to 1.0 for these datasets.

Priors on the limb-darkening coefficients for TESS, NGTS, and EulerCam were calculated using the LDCU code[5], a modified version of the python routine implemented by Espinoza & Jordán (2015) that computes the limb-darkening coefficients and their corresponding uncertainties using a set of stellar intensity profiles accounting for the uncertainties on the stellar parameters. The stellar intensity profiles are generated based on two libraries of synthetic stellar spectra: ATLAS (Kurucz 1979) and PHOENIX (Husser et al. 2013).

As none of the photometric data display significant correlated noise in their datasets around the transits, a periodic Gaussian process term was not included in this fit, simply fitting additional 'jitter' terms in quadrature to both the photometric and spectroscopic data in case the error bars on any of the instruments had been underestimated.

The `juliet` model was run using the `dynesty` nested sampling method with 1100 live points, continuing until the estimated uncertainty in the log evidence was smaller than 0.1. All values and distributions used for the fitted parameters can be found in Table A.1, while the results from the combined fit are displayed in Table 3.

4. Results and discussion

The global model for NGTS-30 b/TOI-4862 b revealed a 98.29838 ± 0.00010 day period Jupiter-sized planet with a radius

---

[5] https://github.com/delinea/LDCU

Table 3. Final results for the exoplanet NGTS-30 b/TOI-4862 b.

Parameter	Value
Fitted parameters	
Orbital period (days)	$98.29838^{+0.00010}_{-0.00009}$
Time of transit T_0 (BJD days)	$2\,459\,287.6000^{+0.0013}_{-0.0014}$
Impact parameter	$0.777^{+0.021}_{-0.027}$
Radius ratio $R_p/R_\star$	$0.1045^{+0.0015}_{-0.0016}$
TESS limb darkening q1	$0.480^{+0.088}_{-0.081}$
TESS limb darkening q2	$0.345^{+0.083}_{-0.075}$
NGTS limb darkening q1	$0.389^{+0.082}_{-0.086}$
NGTS limb darkening q2	$0.306^{+0.084}_{-0.086}$
Eccentricity	$0.294^{+0.014}_{-0.010}$
Argument of periastron (deg)	$3.4^{+4.8}_{-5.8}$
Stellar density (kg m^{-3})	1458^{+157}_{-133}
RV semi-amplitude (m s^{-1})	$46.1^{+1.8}_{-1.8}$
Derived parameters	
Planetary radius (R_J)	$0.928^{+0.032}_{-0.032}$
Planetary mass (M_J)	$0.960^{+0.056}_{-0.056}$
Inclination (deg)	$89.483^{+0.028}_{-0.028}$
Transit duration (h)	$6.13^{+0.27}_{-0.27}$
Semi-major axis (au)	$0.408^{+0.019}_{-0.019}$
Equilibrium temperature peri. (K)	500^{+55}_{-84}
Equilibrium temperature apa. (K)	274^{+30}_{-46}
Instrumental parameters	
TESS offset (ppm)	-33^{+18}_{-17}
TESS jitter (ppm)	$2.9^{+24.8}_{-2.6}$
NGTS offset (ppm)	87^{+20}_{-19}
NGTS jitter (ppm)	4600^{+178}_{-180}
EulerCam offset (ppm)	-1568^{+209}_{-208}
EulerCam jitter (ppm)	872^{+81}_{-73}
CORALIE offset (m s^{-1})	$45576.5^{+6.9}_{-7.3}$
CORALIE jitter (m s^{-1})	$0.08^{+1.70}_{-0.07}$
FEROS offset (m s^{-1})	$45558.1^{+5.7}_{-5.5}$
FEROS jitter (m s^{-1})	$14.0^{+6.3}_{-4.5}$
HARPS offset (m s^{-1})	$45467.3^{+1.5}_{-1.4}$
HARPS jitter (m s^{-1})	$4.5^{+2.4}_{-4.2}$
PFS offset (m s^{-1})	$-13.6^{+1.0}_{-0.9}$
PFS jitter (m s^{-1})	$3.3^{+1.4}_{-1.0}$

of $0.928 \pm 0.032\,R_J$ and mass of 0.960 ± 0.05 day M_J, representing errors in radius and mass of only 3.4% and 5.8%, respectively. The orbit of NGTS-30 b/TOI-4862 b has an eccentricity of $0.294^{+0.014}_{-0.010}$, inclination of 89.483 ± 0.028 deg and semi-major axis of 0.408 ± 0.019 au.

The photometric data around the two fitted transits of TOI-4862 b and the residuals after removing the joint model are shown in Fig. 1. The higher-cadence NGTS and EulerCam data are presented in one minute bins for clarity (in green) and ten minute bins (in black), to align with the TESS data cadence. A 1% transit depth is clearly evident in all datasets, reflecting the obtained radius ratio of $R_p/R_\star = 0.1045 \pm 0.0015$. Meanwhile, the fitted RV data are illustrated in Figs. 9 and 10, showing the phased and time-series data, respectively. The fitted RV model
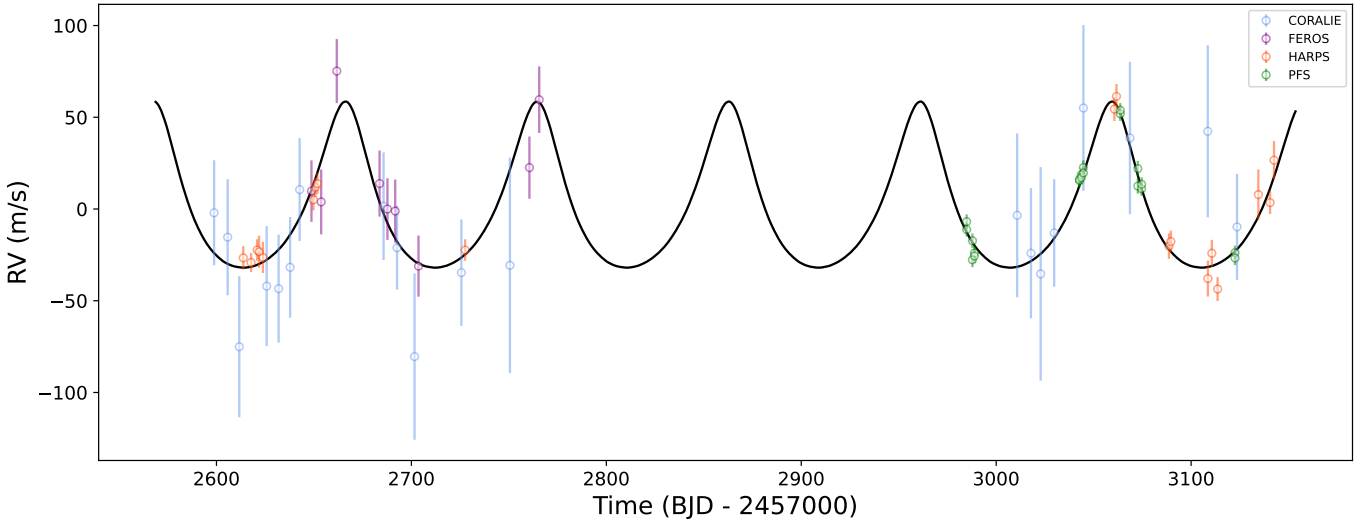
Fig. 10. RV time series (in colour) with the RV model from the joint fit over-plotted in black. CORALIE RVs are shown in blue, FEROS RVs in purple, HARPS RVs in orange, and PFS RVs in green.

shows an amplitude of $K = 46.1 \pm 1.8$ m s^{-1}, and the medium eccentricity of the planet's orbit is clearly evident from the asymmetric shape of the model. Like the photometric data, the RV data from all instruments yield flat residuals after the removal of the joint model. Furthermore, the scatter of all points are comparable to the RV error for each instrument, agreeing with the one-planet hypothesis. The complete set of fitted and derived results for this system can be found in Table 3 and the posterior distributions for all fitted parameters can be found in Fig. B.1.

4.1. Interior modelling

NGTS-30 b/TOI-4862 b is a transiting warm Jupiter with precisely determined mass, radius, and age making it a good candidate to investigate its interior composition. Given its stellar insolation of $3.90 \pm 0.40\ S_\oplus$ and an average equilibrium temperature of 390K, the planet is assumed not to be inflated and thus there is no degeneracy between the heavy element content and the amount of radius inflation. The planetary evolution code `completo` (Mordasini et al. 2012) is used to model the core and the envelope along with a semi-grey atmospheric model. A grid of evolution models assuming no bloating of the planet was built and coupled on this grid with a Bayesian inference model to estimate the heavy element content. The planet is modelled with a core of $10\ M_\oplus$ and an envelope of hydrogen and helium in which heavy elements are homogeneously mixed. The heavy elements are modelled as water following the equation of state AQUA2020 (Haldemann et al. 2020). Hydrogen and helium are modelled with the equation of state from Chabrier & Debras (2021, CMS2019). As shown by Müller et al. (2020), the equation of state CMS2019 is known to lead to smaller radii for a given age and metallicity than the SCvH equation of state (Saumon et al. 1995). Figure C.1 displays the posterior distribution of the heavy element fit for TOI-4862 b. Using this model, the planet was found to have a heavy element mass fraction of $0.23^{+0.05}_{-0.06}$, which corresponds to a mass of $85^{+15}_{-20}\ M_\oplus$: $10\ M_\oplus$ of this mass of heavy element is the core mass, the rest is homogeneously mixed in the envelope. Assuming that the stellar metallicity scales with the iron abundance $Z_\star = 0.0142 \times 10^{[\mathrm{Fe/H}]}$ (Asplund et al. 2009; Miller & Fortney 2011), the heavy element enrichment ($Z_\mathrm{P}/Z_\star$) is 20^{+5}_{-6} and TOI-4862 b is

metal-enriched compared to its host star. This agrees well with the theoretical predictions by Thorngren et al. (2016) assuming Toomre's Q parameter has a value of $Q = 5$ (as with their best-fit model).

4.2. Comparison to the known population

In order to place NGTS-30 b/TOI-4862 b in the context of other giant planet discoveries, the planet was plotted in period-radius and period-mass space in Figs. 11 and 12, respectively. To construct these plots, all planets from the NASA Exoplanet Archive[6] (Akeson et al. 2013) were downloaded. Then a sample was assembled by choosing those that were giant ($0.2R_\mathrm{J} \leq R_\mathrm{P} \leq 13R_\mathrm{J}$), transiting, and had well-constrained masses ($\sigma_{M_\mathrm{P}}/M_\mathrm{P} \leq 25\%$) and radii ($\sigma_{R_\mathrm{P}}/R_\mathrm{P} \leq 8\%$). Plotted in colour are the V-band magnitude (Fig. 11) and the eccentricity (Fig. 12) of this sample. These plots illustrate that TOI-4862 b has a small radius compared to other currently known giant exoplanets of ~100 days, but a mass approximately in the middle of the population. The magnitude of its host star (Vmag = 12.5) places it close to the middle of the range, keeping it within reach of atmospheric characterisation.

4.3. Eccentricity

Figure 12 shows that NGTS-30 b/TOI-4862 b has a moderate eccentricity of 0.294, in line with the median eccentricity for exoplanets with periods greater than ~50 days (n.b. as above, these data were drawn from the NASA Exoplanet Archive[6]). Eccentricity is particularly interesting for warm Jupiters, as there appear to be two distinct groups of eccentricity: higher-mass ($>2\ M_\mathrm{J}$) planets tend to have larger eccentricities, while lower-mass warm Jupiters generally appear to have smaller eccentricities (see Fig. 12). A similar split in eccentricity between high mass ($\geq 4\ M_\mathrm{J}$) and low mass ($<4\ M_\mathrm{J}$) giants was seen by Ribas & Miralda-Escudé (2007) in RV planet discoveries, and they suggested that this pointed towards higher mass warm Jupiters forming from fragmentation of the pre-stellar cloud (in a similar
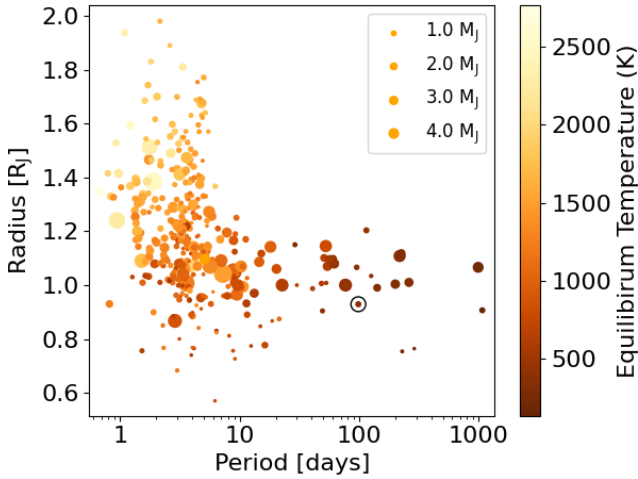
---

[6] https://exoplanetarchive.ipac.caltech.edu/

Fig. 11. Period vs. radius plot for all giant transiting exoplanets ($0.2\,R_{\rm J} \leq R_{\rm P} \leq 13\,R_{\rm J}$) with well-constrained masses ($\sigma_{M_{\rm P}}/M_{\rm P} \leq 25\%$) and radii ($\sigma_{R_{\rm P}}/R_{\rm P} \leq 8\%$). Individual points are colour-coded by the V-magnitude of the host star. TOI-4862 b is circled in black.
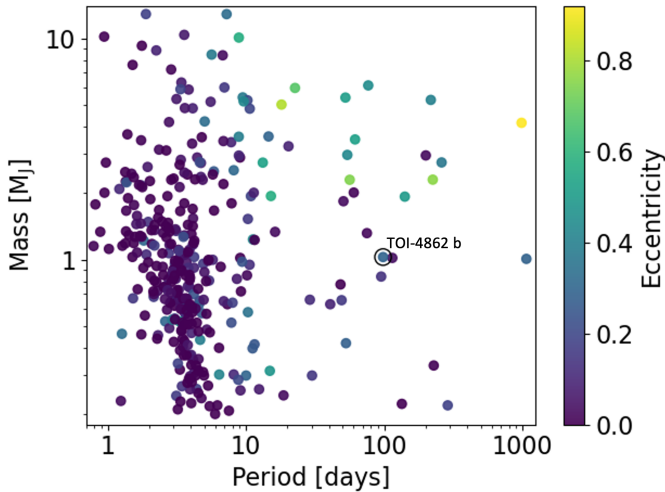

Fig. 12. Period vs. mass plot for all transiting giant exoplanets ($0.2\,R_{\rm J} \leq R_{\rm P} \leq 13\,R_{\rm J}$) with well-constrained masses ($\sigma_{M_{\rm P}}/M_{\rm P} \leq 25\%$) and radii ($\sigma_{R_{\rm P}}/R_{\rm P} \leq 8\%$). Individual points are colour-coded by the planetary eccentricity, illustrating a general trend towards higher eccentricities at longer periods. TOI-4862 b is circled in black.

manner to binary stars) and lower-mass warm Jupiters forming via more classical core accretion mechanisms (e.g. Safronov 1972; Lissauer 1993; Pollack et al. 1996). However, this discrepancy could also be caused by massive planets remaining stable on eccentric orbits while lower-mass planets become unstable (e.g. Chatterjee et al. 2008). One way to further investigate the past evolutionary history of this planet would be to measure the spin-orbit angle of TOI-4862 b, which can be achieved through observations of the Rossiter-McLaughlin effect (e.g. Rossiter 1924; McLaughlin 1924; Ohta et al. 2005; Cegla et al. 2016; Wang et al. 2021; Rice et al. 2021; Bourrier et al. 2021). Such a measurement would provide a cornerstone constraint in an almost entirely unpopulated region of parameter space for warm Jupiters with 2D spin-orbit measurements – at very long orbital periods and wide star-planet separations (Rice et al. 2022; Albrecht et al. 2022). Using Eq. (40) from Winn (2010) gives an estimated value for the Rossiter–McLaughlin effect of $24\,{\rm m\,s^{-1}}$.

4.4. Equilibrium temperature

The current eccentricity of NGTS-30 b/TOI-4862 b's orbit coupled with its long period implies that interesting changes occur in its equilibrium temperature over the course of its orbit. Given its similarity to Jupiter, the equilibrium temperature of TOI-4862 b can be estimated by assuming a Jupiter-like albedo of 0.343 and generating upper and lower bounds by assuming bond albedos of A = 0 and A = 0.686 (double that of Jupiter). Using Eq. (1) (which takes into consideration the eccentricity of the planet but assumes instant heat distribution and a vanishingly small heat capacity) the planetary equilibrium temperature was calculated to vary from 500^{+55}_{-84} K at periastron to 274^{+30}_{-46} K at apastron. Although in reality the temperature changes over the course of the planet's orbit will be tempered by the atmospheric heat capacity and redistribution of heat in the planet's atmosphere, the dramatic change in temperature over the course of this eccentric wide orbit illustrates the unusual and evolving environment faced by this exoplanet.

$$T_{\rm eq} = T_{\rm eff}(1 - A)^{1/4} \sqrt{\frac{R_*}{2a(1 \pm e)}}. \tag{1}$$

4.5. Prospects for atmospheric characterisation

NGTS-30 b/TOI-4862 b joins a small but growing population of intermediate insolation giant exoplanets that are amenable to atmospheric characterisation using transmission spectroscopy. These warm and temperate gas giants are the missing link between the cold gas giants of the Solar System and the well-characterised hot Jupiter population. Because warm and temperate gas giants exist at wide enough orbits to avoid tidal circularisation, information on their migration history is retained in their eccentricity (Dawson & Johnson 2018). By exploring links between atmospheric composition and the mass, age, period, eccentricity, and planetary companions of warm and temperate gas giants we can hope to understand the migration and formation history of hot Jupiters.

The atmospheres of temperate gas giants like NGTS-30 b/TOI-4862 b (<500 K) are particularly interesting as they can shed light on a cooler physical and chemical atmospheric regime than has been previously studied. In particular observationally unconstrained key transitions in nitrogen chemistry (Fortney et al. 2020; Hu 2021; Ohno & Fortney 2023) and aerosol properties (Gao et al. 2017; Brande et al. 2024) are predicted to occur in this parameter space. The eccentricity of NGTS-30 b/TOI-4862 b means it may probe these transitions during its orbit.

With a transmission spectroscopy metric of 16, NGTS-30 b/TOI-4862 b is amenable to characterisation with JWST, greater than the cycle 2 temperate gas giant target PH-2b (PID 3235). This allows for the measurement of chemical composition through the C/N/O ratio, which can therefore be related to the planet's formation and migration history (Mordasini et al. 2012; Piso et al. 2016; Cridland et al. 2020; Ohno & Fortney 2023). The young age and well-constrained moderate eccentricity of NGTS-30 b/TOI-4862 b makes it a unique addition to the temperate gas giant population, which is otherwise composed of evolved planets of lower or uncertain eccentricity.

4.6. Age

Another key parameter for anchoring the formation and evolution of warm Jupiters is age. In this analysis NGTS-30 b/TOI-4862 b and its host star were found to have an age of 1.1 ± 0.4 Gyr
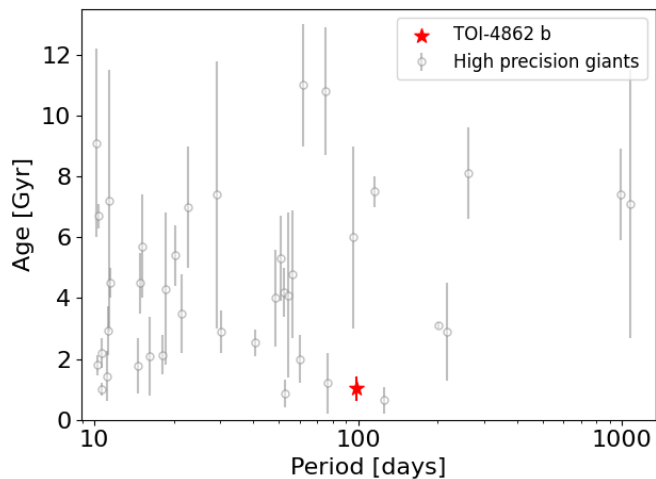
Fig. 13. Period vs. age plot for all giant exoplanets ($0.2\,R_J \leq R_P \leq 13\,R_J$) with well-constrained masses ($\sigma_{M_P}/M_P \leq 25\%$) and radii ($\sigma_{R_P}/R_P \leq 8\%$), periods of >10 days, and errors in age of $\sigma_{\mathrm{Age}}/\mathrm{Age} \leq 100\%$. TOI-4862 b is shown by the red star, illustrating its position as one of the youngest warm Jupiters to date with a well-constrained age. The large age errors of most long-period giants are also evident.

based on the star's $v \sin i$ value, making it a fairly young, or 'adolescent' system (n.b. 'young' exoplanets are often deemed to be those with ages of ≤1 Gyr – see for example Battley et al. 2020). In order to place this discovery in the context of the wider warm Jupiter population, the aforementioned sample of high precision giant exoplanets, restricted to those giants with periods greater than 10 days and age errors of $\sigma_{\mathrm{Age}}/\mathrm{Age} \leq 100\%$, was plotted in period-age parameter space in Fig. 13. What is immediately obvious is that most long-period planets have very poorly constrained ages, severely hampering modelling of their evolution through time. In order to form a reliable picture of how long-period exoplanets evolve with time, it is imperative that better age constraints are put on these planets via carefully ageing their host stars. In this regard TOI-4862 is better than most, with age errors of only 400 Myr thanks to a clear $v \sin i$ signal with which to conduct gyrochronology. The 1.1 Gyr age makes TOI-4862 b one of the youngest long-period exoplanets found to date with both a precise mass and radius, providing the community with a cornerstone system with which to probe the early evolution of warm Jupiters. Furthermore, as discussed in Sect. 3.1, there is marginal evidence from the WASP data that the rotation period may be as low as 7.5 ± 3 days (at the shorter end of the $v \sin i$ constraints), suggesting that the planet is even younger. Placing further constraints on the age of this system and/or acquiring additional signs of youth for TOI-4862 would be very valuable for more precisely anchoring this planet within this dynamic epoch of evolution.

5. Conclusions

This paper has presented the discovery and characterisation of the newly discovered long-period exoplanet NGTS-30 b/TOI-4862 b, an adolescent warm Jupiter on a 98.3-day orbit around the *G*-type star TOI-4862. This planet has a radius of $0.928 \pm 0.032\,R_J$, a mass of $0.960 \pm 0.056\,M_J$, and an orbital eccentricity of $0.294^{+0.014}_{-0.010}$. NGTS-30 b/TOI-4862 b was discovered through a single transit from TESS before its true period was determined through a combination of photometric monitoring with NGTS and spectrographic RV measurements from CORALIE, FEROS,

HARPS, and PFS, which allowed tight constraints to be placed on the planetary mass. The star's age of 1.1 Gyr makes NGTS-30 b/TOI-4862 b one of the youngest warm Jupiters found, adding a crucial new system with which to understand the evolution timescale of such planets. Further observations of the spin-orbit angle and the atmosphere of this planet will help further define the migration history and composition of this interesting system.

References

Akeson, R. L., Chen, X., Ciardi, D., et al. 2013, PASP, 125, 989
Albrecht, S. H., Dawson, R. I., & Winn, J. N. 2022, PASP, 134, 082001
Asplund, M., Grevesse, N., Sauval, A. J., & Scott, P. 2009, ARA&A, 47, 481
Battley, M. P., Pollacco, D., & Armstrong, D. J. 2020, MNRAS, 496, 1197
Bitsch, B., Izidoro, A., Johansen, A., et al. 2019, A&A, 623, A88
Blanco-Cuaresma, S., Soubiran, C., Heiter, U., & Jofré, P. 2014, A&A, 569, A111
Boley, A. C., Contreras, A. P. G., & Gladman, B. 2016, ApJ, 817, L17
Borgniet, S., Lagrange, A.-M., Meunier, N., et al. 2019, A&A, 621, A87
Borucki, W. J., & Summers, A. L. 1984, Icarus, 58, 121
Boss, A. P. 1997, Science, 276, 1836
Bourrier, V., Lovis, C., Cretignier, M., et al. 2021, A&A, 654, A152
Brahm, R., Jordán, A., & Espinoza, N. 2017, PASP, 129, 034002
Brahm, R., Ulmer-Moll, S., Hobson, M. J., et al. 2023, AJ, 165, 227
Brande, J., Crossfield, I. J. M., Kreidberg, L., et al. 2024, ApJ, 961, L23
Bryant, E. M., Bayliss, D., McCormac, J., et al. 2020, MNRAS, 494
Buchhave, L. A., Bakos, G. A., Hartman, J. D., et al. 2010, ApJ, 720, 1118
Buchhave, L. A., Bizzarro, M., Latham, D. W., et al. 2014, Nature, 509, 593
Butler, R. P., Marcy, G. W., Williams, E., et al. 1996, PASP, 108, 500
Caldwell, D. A., Tenenbaum, P., Twicken, J. D., et al. 2020, RNAAS, 4, 201
Cegla, H. M., Lovis, C., Bourrier, V., et al. 2016, A&A, 588, A127
Chabrier, G., & Debras, F. 2021, ApJ, 917, 4
Chatterjee, S., Ford, E. B., Matsumura, S., & Rasio, F. A. 2008, ApJ, 686, 580

Cooke, B. F., Pollacco, D., West, R., McCormac, J., & Wheatley, P. J. 2018, A&A, 619, A175

Cooke, B. F., Pollacco, D., Anderson, D. R., et al. 2020, MNRAS, 500, 5088

Crane, J. D., Shectman, S. A., & Butler, R. P. 2006, Proc. SPIE, 6269, 626931

Crane, J. D., Shectman, S. A., Butler, R. P., Thompson, I. B., & Burley, G. S. 2008, Proc. SPIE, 7014, 701479

Crane, J. D., Shectman, S. A., Butler, R. P., et al. 2010, Proc. SPIE, 7735, 773553

Cridland, A. J., van Dishoeck, E. F., Alessi, M., & Pudritz, R. E. 2020, A&A, 642, A229

Dalba, P. A., Gupta, A. F., Rodriguez, J. E., et al. 2020, AJ, 159, 241

Dawson, R. I., & Johnson, J. A. 2018, ARA&A, 56, 175

Espinoza, N., & Jordán, A. 2015, MNRAS, 450, 1879

Espinoza, N., Kossakowski, D., & Brahm, R. 2019, MNRAS, 490, 2262

Fabrycky, D., & Tremaine, S. 2007, ApJ, 669, 1298

Faria, J. P., Santos, N. C., Figueira, P., & Brewer, B. J. 2018, J. Open Source Softw., 3, 487

Foreman-Mackey, D., Agol, E., Ambikasaran, S., & Angus, R. 2017, AJ, 154, 220

Fortney, J. J., Visscher, C., Marley, M. S., et al. 2020, AJ, 160, 288

Fulton, B. J., Petigura, E. A., Blunt, S., & Sinukoff, E. 2018, PASP, 130, 044504

Furész, G. 2008, PhD Thesis, University of Szeged, Hungary

Gaia Collaboration (Prusti, T., et al.) 2016, A&A, 595, A1

Gao, P., Marley, M. S., Zahnle, K., Robinson, T. D., & Lewis, N. K. 2017, AJ, 153, 139

Gill, S., Wheatley, P. J., Cooke, B. F., et al. 2020, ApJ, 898, L11

Gray, R. O. 1999, Astrophysics Source Code Library [record ascl:9910.002]

Grieves, N., Bouchy, F., Ulmer-Moll, S., et al. 2022, A&A, 668, A29

Guerrero, N. M., Seager, S., Huang, C. X., et al. 2021, ApJS, 254, 39

Gupta, A. F., Jackson, J. M., Hébrard, G., et al. 2023, AJ, 165, 234

Gustafsson, B., Edvardsson, B., Eriksson, K., et al. 2008, A&A, 486, 951

Haldemann, J., Alibert, Y., Mordasini, C., & Benz, W. 2020, A&A, 643, A105

Hog, E., Fabricius, C., Makarov, V. V., et al. 2000, A&A, 355, L27

Hu, R. 2021, ApJ, 921, 27

Husser, T. O., Wende-von Berg, S., Dreizler, S., et al. 2013, A&A, 553, A6

Ida, S., & Lin, D. N. 2010, ApJ, 719, 810

Jenkins, J. M. 2002, ApJ, 575, 493

Jenkins, J. M., Twicken, J. D., McCauliff, S., et al. 2016, Proc. SPIE, 9913, 99133E

Jenkins, J. M., Tenenbaum, P., Seader, S., et al. 2020, Kepler Science Document KSCI-19081-003, 9

Kaufer, A., Stahl, O., Tubbesing, S., et al. 1999, The Messenger, 95, 8

Kipping, D. M. 2013, MNRAS, 435, 2152

Kozai, Y. 1962, AJ, 67, 591

Kreidberg, L. 2015, PASP, 127, 1161

Kunimoto, M., Tey, E., Fong, W., et al. 2023, RNAAS, 7, 28

Kurucz, R. L. 1979, ApJS, 40, 1

Kurucz, R. L. 1992, in The Stellar Populations of Galaxies, eds. B. Barbuy, & A. Renzini (Dordrecht: Kluwer)

Lang, D., Hogg, D. W., Mierle, K., Blanton, M., & Roweis, S. 2010, AJ, 139, 1782

Lendl, M., Anderson, D. R., Collier-Cameron, A., et al. 2012, A&A, 544, A72

Lendl, M., Bouchy, F., Gill, S., et al. 2020, MNRAS, 492, 1761

Li, J., Tenenbaum, P., Twicken, J. D., et al. 2019, PASP, 131, 024506

Lidov, M. 1962, Planet. Space Sci., 9, 719

Lin, D. N. C., & Papaloizou, J. 1986, ApJ, 309, 846

Lissauer, J. J. 1993, ARA&A, 31, 129

Lomb, N. 1976, Astrophys. Space Sci., 39, 447

Lovis, C., & Pepe, F. 2007, A&A, 468, 1115

Mamajek, E. E., & Hillenbrand, L. A. 2008, ApJ, 687, 1264

Mann, C. R., Dalba, P. A., Lafrenière, D., et al. 2023, AJ, 166, 239

Marmier, M., Ségransan, D., Udry, S., et al. 2013, A&A, 551, A90

Maxted, P. F. L., Anderson, D. R., Collier Cameron, A., et al. 2011, PASP, 123, 547

McLaughlin, D. B. 1924, ApJ, 60, 22

Miller, N., & Fortney, J. J. 2011, ApJ, 736, L29

Mireles, I., Dragomir, D., Osborn, H. P., et al. 2023, ApJ, 954, L15

Montalto, M., Borsato, L., Granata, V., et al. 2020, MNRAS, 498, 1726

Mordasini, C., Alibert, Y., Klahr, H., & Henning, T. 2012, A&A, 547, A111

Mordasini, C., Mollière, P., Dittkrist, K.-M., Jin, S., & Alibert, Y. 2015, Int. J. Astrobiol., 14, 201

Müller, S., & Helled, R. 2023, Front. Astron. Space Sci., 10, 1179000

Müller, S., Ben-Yami, M., & Helled, R. 2020, ApJ, 903, 147

Ohno, K., & Fortney, J. J. 2023, ApJ, 956, 125

Ohta, Y., Taruya, A., & Suto, Y. 2005, ApJ, 622, 1118

Osborn, H. P., Armstrong, D. J., Brown, D. J. A., et al. 2016, MNRAS, 457, 2273

Osborn, H. P., Bonfanti, A., Gandolfi, D., et al. 2022, A&A, 664, A156

Osborn, H. P., Nowak, G., Hébrard, G., et al. 2023, MNRAS, 523, 3069

Owen, J. E. 2019, Annu. Rev. Earth Planet. Sci., 47, 67

Pepe, F., Mayor, M., Galland, F., et al. 2002, A&A, 388, 632

Piso, A.-M. A., Pegues, J., & Öberg, K. I. 2016, ApJ, 833, 203

Pollacco, D. L., Skillen, I., Collier Cameron, A., et al. 2006, PASP, 118, 1407

Pollack, J. B., Hubickyj, O., Bodenheimer, P., et al. 1996, Icarus, 124, 62

Pont, F., Knutson, H., Gilliland, R. L., Moutou, C., & Charbonneau, D. 2008, MNRAS, 385, 109

Queloz, D., Mayor, M., Weber, L., et al. 2000, A&A, 354, 99

Ribas, I., & Miralda-Escudé, J. 2007, A&A, 464, 779

Rice, M., Wang, S., Howard, A. W., et al. 2021, AJ, 162, 182

Rice, M., Wang, S., Wang, X.-Y., et al. 2022, AJ, 164, 104

Ricker, G. R., Winn, J. N., Vanderspek, R., et al. 2014, JATIS, 1, 014003

Rossiter, R. A. 1924, ApJ, 60, 15

Safronov, V. S. 1972, Evolution of the Protoplanetary Cloud and Formation of the Earth and Planets (Jerusalem: Israel Program for Scientific Translations)

Saumon, D., Chabrier, G., & van Horn, H. M. 1995, ApJS, 99, 713

Scargle, J. 1982, ApJ, 263, 835

Schlegel, D. J., Finkbeiner, D. P., & Davis, M. 1998, ApJ, 500, 525

Seager, S., & Sasselov, D. D. 2000, ApJ, 537, 916

Showman, A. P., Tan, X., & Parmentier, V. 2020, Space Sci. Rev., 216, 139

Skrutskie, M. F., Cutri, R. M., Stiening, R., et al. 2006, AJ, 131, 1163

Smith, J. C., Stumpe, M. C., Van Cleve, J. E., et al. 2012, PASP, 124, 1000

Smith, A. M. S., Eigmüller, P., Gurumoorthy, R., et al. 2020, Astron. Nachr., 341, 273

Speagle, J. S. 2020, MNRAS, 493, 3132

Stassun, K. G., & Torres, G. 2016, AJ, 152, 180

Stassun, K. G., Collins, K. A., & Gaudi, B. S. 2017, AJ, 153, 136

Stassun, K. G., Corsaro, E., Pepper, J. A., & Gaudi, B. S. 2018, AJ, 155, 22

Stassun, K. G., Oelkers, R. J., Paegert, M., et al. 2019, AJ, 158, 138

Stumpe, M. C., Smith, J. C., Van Cleve, J. E., et al. 2012, PASP, 124, 985

Stumpe, M. C., Smith, J. C., Catanzarite, J. H., et al. 2014, PASP, 126, 100

Thorngren, D. P., Fortney, J. J., Murray-Clay, R. A., & Lopez, E. D. 2016, ApJ, 831, 64

Tokovinin, A. 2018, PASP, 130, 035002

Torres, G., Andersen, J., & Giménez, A. 2010, A&ARv, 18, 67

Twicken, J. D., Catanzarite, J. H., Clarke, B. D., et al. 2018, PASP, 130, 064502

Udry, S., Mayor, M., & Santos, N. C. 2003, A&A, 407, 369

Ulmer-Moll, S., Lendl, M., Gill, S., et al. 2022, A&A, 666, A46

Ulmer-Moll, S., Osborn, H. P., Tuson, A., et al. 2023, A&A, 674, A43

Villanueva, S., Dragomir, D., & Gaudi, B. S. 2019, AJ, 157, 84

Wang, S., Winn, J. N., Addison, B. C., et al. 2021, AJ, 162, 50

Ward, W. R. 1986, Icarus, 67, 164

Wheatley, P. J., West, R. G., Goad, M. R., et al. 2018, MNRAS, 475, 4476

Winn, J. 2010, in Exoplanets, ed. S. Seager (Tucson: University of Arizona Press), 55

Wright, E. L., Eisenhardt, P. R. M., Mainzer, A. K., et al. 2010, AJ, 140, 1868

Wu, Y., & Lithwick, Y. 2011, ApJ, 735, 109

Ziegler, C., Tokovinin, A., Briceño, C., et al. 2019, AJ, 159, 19

[1] Observatoire Astronomique de l'Université de Genève, Chemin Pegasi 51, 1290 Versoix, Switzerland
e-mail: matthew.battley@unige.ch

[2] Center for Astrophysics | Harvard & Smithsonian, 60 Garden Street, Cambridge, MA 02138, USA

[3] Physikalisches Institut, University of Bern, Gesellsschaftstrasse 6, 3012 Bern, Switzerland

[4] Department of Physics, University of Warwick, Gibbet Hill Road, Coventry CV4 7AL, UK

[5] Centre for Exoplanets and Habitability, University of Warwick, Gibbet Hill Road, Coventry CV4 7AL, UK

[6] Facultad de Ingeniería y Ciencias, Universidad Adolfo Ibáñez, Av. Diagonal las Torres 2640, Peñalolén, Santiago, Chile

[7] Millennium Institute for Astrophysics, Chile

[8] Data Observatory Foundation, Santiago, Chile

[9] Department of Physics and Astronomy, Vanderbilt University, Nashville, TN 37235, USA

[10] Astrophysics Group, Keele University, Staffordshire, ST5 5BG, UK

[11] Departamento de Astronomía, Universidad de Chile, Casilla 36-D, Santiago, Chile

[12] Department of Physics, Engineering and Astronomy, Stephen F. Austin State University, 1936 North St, Nacogdoches, TX 75962, USA

[13] Instituto de Astronomía, Universidad Católica del Norte, Angamos 0610, 1270709, Antofagasta, Chile

[14] Las Campanas Observatory, Carnegie Institution for Science, Colina el Pino, Casilla 601 La Serena, Chile

[15] School of Physics and Astronomy, University of Leicester, Leicester LE1 7RH, UK

[16] Earth and Planets Laboratory, Carnegie Institution for Science, 5241 Broad Branch Road, NW, Washington, DC 20015, USA

[17] Caltech/IPAC-NASA Exoplanet Science Institute, 770 S. Wilson Avenue, Pasadena, CA 91106, USA

[18] The Observatories of the Carnegie Institution for Science, 813 Santa Barbara St., Pasadena, CA 91101, USA

[19] Department of Astronomy and Astrophysics, University of California, Santa Cruz, CA 95064, USA

[20] Department of Physics and McDonnell Center for the Space Sciences, Washington University, St. Louis, MO 63130, USA

[21] Astronomy Unit, Queen Mary University of London, Mile End Road, London E1 4NS, UK

[22] European Space Agency (ESA), European Space Research and Technology Centre (ESTEC), Keplerlaan 1, 2201 AZ Noordwijk, The Netherlands

[23] Max-Planck-Institut für Astronomie, Königstuhl 17, 69117 Heidelberg, Germany

[24] Instituto de Estudios Astrofísicos, Facultad de Ingeniería y Ciencias, Universidad Diego Portales, Av. Ejército 441, Santiago, Chile

[25] Centro de Astrofísica y Tecnologías Afines (CATA), Casilla 36-D, Santiago, Chile

[26] Department of Physics and Kavli Institute for Astrophysics and Space Research, Massachusetts Institute of Technology, 77 Massachusetts Ave, Cambridge, MA 02139, USA

[27] NASA Goddard Space Flight Center, 8800 Greenbelt Road, Greenbelt, MD 20771, USA

[28] Department of Astronomy, Yale University, New Haven, CT 06511, USA

[29] Center for Data Intensive and Time Domain Astronomy, Department of Physics and Astronomy, Michigan State University, East Lansing, MI 48824, USA

[30] Department of Earth, Atmospheric and Planetary Sciences, Massachusetts Institute of Technology, Cambridge, MA 02139, USA

[31] Department of Aeronautics and Astronautics, MIT, 77 Massachusetts Avenue, Cambridge, MA 02139, USA

[32] Insitute of Planetary Research, German Aerospace Center (DLR), Rutherfordstr. 2, 12489 Berlin, Germany

[33] Earth and Planets Laboratory, Carnegie Institution for Science, 5241 Broad Branch Rd NW, Washington, DC 20015, USA

[34] NASA Ames Research Center, Moffett Field, CA 94035, USA

[35] Astrophysics Research Centre, Queen's University Belfast, Belfast BT7 1NN, UK

[36] Department of Astrophysical Sciences, Princeton University, Princeton, NJ 08544, USA

Appendix A: Joint modelling priors

Table A.1. Priors for the joint modelling of photometric and RV data.

Parameter	Distribution	Value
Orbital Period [days]	Normal	(98.3, 1.5)
Mid-transit time T_0 [days]	Normal	(2459287.603184,0.2)
Impact Parameter	Uniform	(0, 1)
Radius ratio $R_p/R_\star$	Uniform	(0,1)
TESS limb darkening q1	Normal	(0.363879, 5 x 0.017721)
TESS limb darkening q2	Normal	(0.291963, 5 x 0.017069)
NGTS limb darkening q1	Normal	(0.417738, 5 x 0.017562)
NGTS limb darkening q2	Normal	(0.309776, 5 x 0.017689)
EulerCam limb darkening q1	Normal	(0.420494, 5 x 0.017562)
EulerCam limb darkening q2	Normal	(0.310417, 5 x 0.017689)
Eccentricity	Uniform	(0.0, 0.8)
Argument of periastron [deg]	Uniform	(0, 360)
Stellar density (kg.m^{-3})	Normal	(1741.325, 200)
TESS offset [ppm]	Normal	(0.0,100000)
TESS jitter [ppm]	LogUniform	(0.1, 1000)
NGTS offset [ppm]	Normal	(0.,100000)
NGTS jitter [ppm]	LogUniform	(0.1, 10000)
EulerCam offset [ppm]	Normal	(0.,100000)
EulerCam jitter [ppm]	LogUniform	(0.1, 10000)
RV Semi-Amplitude [m.s^{-1}]	Uniform	(0,100)
Spectrograph Jitters [m.s^{-1}]	LogUniform	(0.001,100)
CORALIE offset [m.s^{-1}]	Uniform	[40000,50000]
FEROS offset [m.s^{-1}]	Uniform	[40000,50000]
HARPS offset [m.s^{-1}]	Uniform	[40000,50000]
PFS offset [m.s^{-1}]	Uniform	[-100,100]

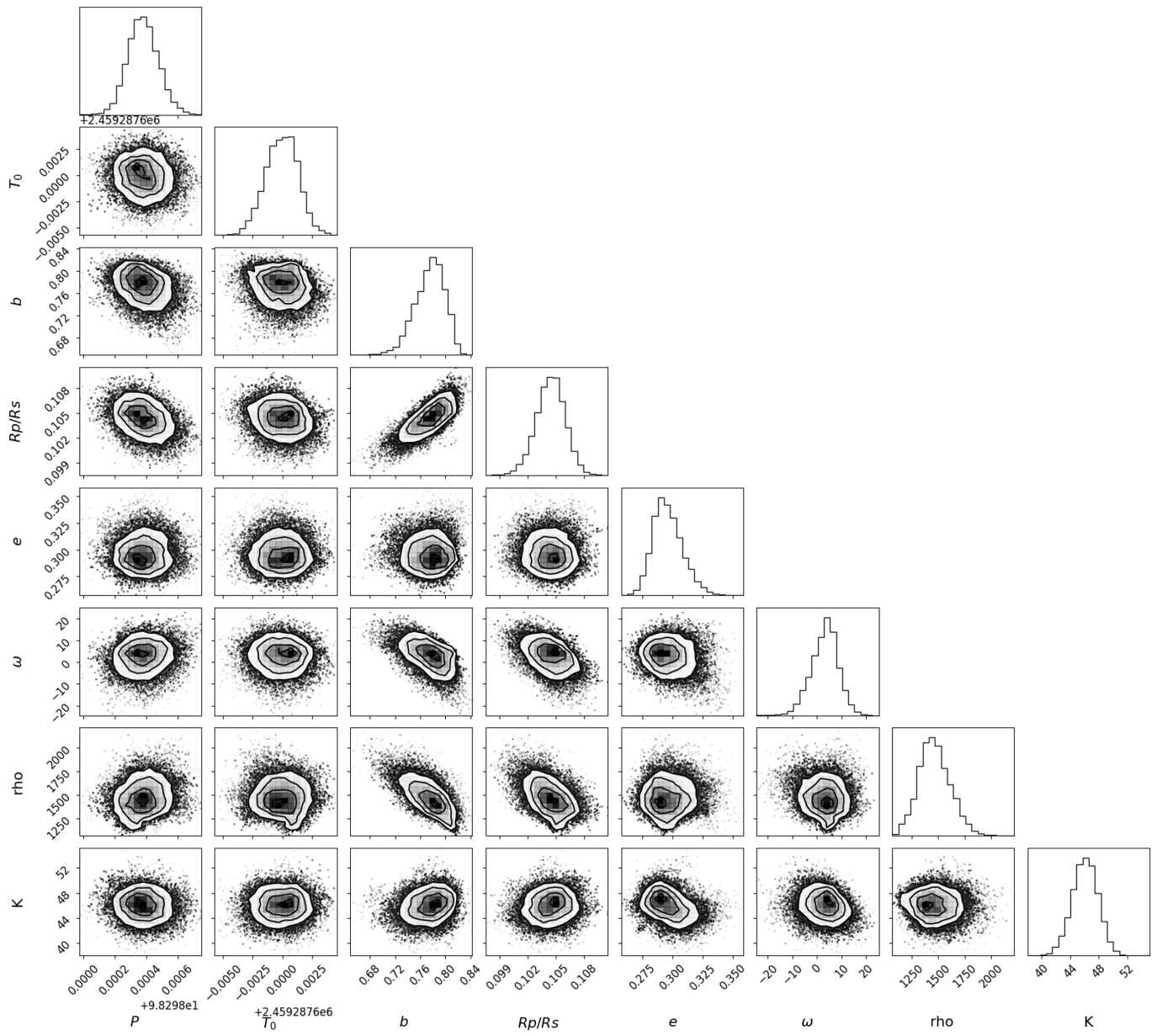## Appendix B: Joint modelling posterior distributions

Fig. B.1. Posterior distribution for fitted parameters from the joint fit of NGTS-30 b/TOI-4862 b.

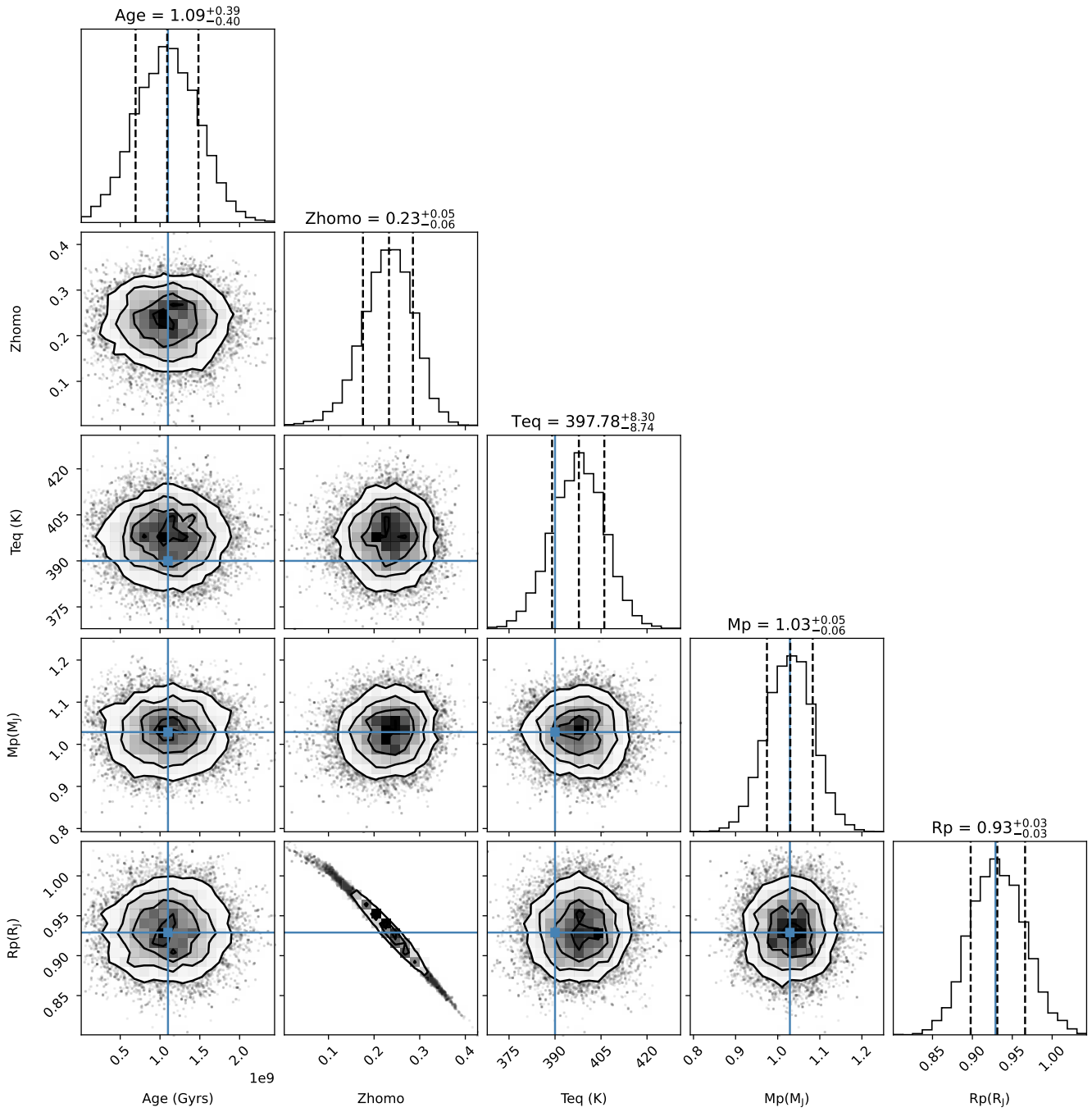## Appendix C: Interior modelling posterior distributions

Fig. C.1. Posterior probability distribution for the interior modelling of TOI-4862 b. The age is in years, Zhomo (the homogeneous metallicity) corresponds to the fraction of heavy elements in the atmosphere, and the planetary mass and radius are in Jupiter units. Blue lines mark the mean values for each parameter.